

Nanoscale thermal imaging of dissipation in quantum systems

D. Halbertal¹, J. Cuppens^{1,2}, M. Ben Shalom^{3,4}, L. Embon^{1,†}, N. Shadmi⁵, Y. Anahory¹, H. R. Naren¹, J. Sarkar¹, A. Uri¹, Y. Ronen¹, Y. Myasoedov¹, L. S. Levitov⁶, E. Joselevich⁵, A. K. Geim^{3,4} & E. Zeldov¹

Energy dissipation is a fundamental process governing the dynamics of physical, chemical and biological systems. It is also one of the main characteristics that distinguish quantum from classical phenomena. In particular, in condensed matter physics, scattering mechanisms, loss of quantum information or breakdown of topological protection are deeply rooted in the intricate details of how and where the dissipation occurs. Yet the microscopic behaviour of a system is usually not formulated in terms of dissipation because energy dissipation is not a readily measurable quantity on the micrometre scale. Although nanoscale thermometry has gained much recent interest^{1–15}, existing thermal imaging methods are not sensitive enough for the study of quantum systems and are also unsuitable for the low-temperature operation that is required. Here we report a nano-thermometer based on a superconducting quantum interference device with a diameter of less than 50 nanometres that resides at the apex of a sharp pipette: it provides scanning cryogenic thermal sensing that is four orders of magnitude more sensitive than previous devices—below $1\ \mu\text{K Hz}^{-1/2}$. This non-contact, non-invasive thermometry allows thermal imaging of very low intensity, nanoscale energy dissipation down to the fundamental Landauer limit^{16–18} of 40 femtowatts for continuous readout of a single qubit at one gigahertz at 4.2 kelvin. These advances enable the observation of changes in dissipation due to single-electron charging of individual quantum dots in carbon nanotubes. They also reveal a dissipation mechanism attributable to resonant localized states in graphene encapsulated within hexagonal boron nitride, opening the door to direct thermal imaging of nanoscale dissipation processes in quantum matter.

Investigation of energy dissipation on the nanoscale is of major fundamental interest for a wide range of disciplines, ranging from biological processes, through chemical reactions, to energy-efficient computing^{1–5}. Study of dissipation mechanisms in quantum systems is of particular importance because dissipation demolishes quantum information. In order to preserve a quantum state, the dissipation has to be extremely weak and hence hard to measure. As a figure of merit for detection of low-power dissipation in quantum systems¹⁶, we consider an ideal qubit operating at a typical read-out frequency of 1 GHz. Landauer's principle states that the lowest bound on energy dissipation in an irreversible qubit operation is $E_0 = k_B T \ln 2$, where k_B is Boltzmann's constant and T is the temperature^{17,18}. At $T = 4.2\ \text{K}$, $E_0 = 4 \times 10^{-23}\ \text{J}$, several orders of magnitude below both the $10^{-19}\ \text{J}$ of dissipation per logical operation in present-day superconducting electronics and the $10^{-15}\ \text{J}$ in CMOS devices^{19,20}. Hence the power dissipated by an ideal qubit operating at a read-out rate of $f = 1\ \text{GHz}$ will be as low as $P = E_0 f = 40.2\ \text{fW}$. The resulting temperature increase of the qubit will depend on its size and the thermal properties of the substrate. For example, a $120\ \text{nm} \times 120\ \text{nm}$ device on a $1\text{-}\mu\text{m}$ -thick SiO_2/Si substrate dissipating $40\ \text{fW}$ will heat up by about $3\ \mu\text{K}$ (Fig. 1). Such signals are several orders of magnitude below the best sensitivity

(several $\text{mK Hz}^{-1/2}$) of any of the existing imaging techniques^{1–15} (Fig. 1a): these include radiation-based thermometry using infrared⁶ (IR), fluorescence in nanodiamonds^{4,7,8}, Raman spectroscopy⁹, scanning near-field optical microscopy¹⁰ (SNOM), or the electron beam induced plasmons in transmission electron microscopy⁵ (TEM), and atomic force microscopy (AFM) equipped with thermocouple (TC SThM) or resistive (Res. SThM) thermometers^{10–15}. Moreover, none of the existing imaging techniques has been demonstrated to operate at the low temperatures that are essential for study of quantum systems.

Superconducting junctions are commonly used as highly sensitive thermometers^{2,21}, relying on the strong temperature dependence of their critical current $I_c(T)$, which in the vicinity of the critical temperature T_c can be approximated by $I_c(T) \approx I_0(1 - T/T_c)$. Conventional junction configurations, however, are not suitable for scanning probe thermometry owing to their planar geometry and strong thermal coupling to the substrate.

Here we introduce a non-contact cryogenic scanning probe microscopy technique based on a superconducting quantum interference device (SQUID) positioned on a tip^{22,23}. We utilize a novel approach in which either a single Pb ($T_c = 7.2\ \text{K}$) superconducting junction or a SQUID is fabricated on the apex of a sharp quartz pipette (SQUID on tip, SOT), and can be made as small as a few tens of nanometres in diameter (Supplementary Information section S1). Figure 1b shows a scanning electron microscopy (SEM) image of a thermometer using this SQUID-on-tip technique (that is, a tSOT) with an effective diameter of $46\ \text{nm}$, as determined from its quantum interference pattern. Similar SOT devices have previously been reported^{22,23} to be extremely sensitive magnetic sensors, reaching a magnetic spin sensitivity below $0.4\ \mu_B\ \text{Hz}^{-1/2}$. The electrical characteristics of the tSOT (Fig. 1c) show the current through the sensor (I_{SOT}) versus externally applied bias current (I_{bias}) at various temperatures (see electrical diagram in Supplementary Fig. 1c). For $I_{\text{SOT}} < I_c$, essentially all the applied current flows through the tSOT, while at higher bias a substantial part of the current diverts to a parallel shunt resistor. When biasing the tSOT at $I_{\text{bias}} > I_c$ (dashed line in Fig. 1c), the temperature dependence of $I_{\text{SOT}}(T)$ gives rise to a thermal response $dI_{\text{SOT}}/dT = -9.5\ \mu\text{A K}^{-1}$ (Supplementary Fig. 1b); when this is combined with the very low white noise of the tSOT ($S_I^{1/2} = 8.3\ \text{pA Hz}^{-1/2}$; Supplementary Fig. 1c) it translates into a remarkably low thermal noise of $S_T^{1/2} = 870\ \text{nK Hz}^{-1/2}$, an improvement of four orders of magnitude over existing thermal imaging methods (Fig. 1a).

To enable effective thermal imaging, the thermal properties of the sensor, including its coupling to the sample, are crucial. For non-invasive imaging, the thermal resistance between the sensor and the investigated device, R_{sd} , has to be considerably larger than the thermal resistance between the device and the bulk of its substrate, R_{db} (Fig. 1d). On the other hand, in order for the temperature of the sensor T_s to accurately describe the local temperature of the device T_d , a high

¹Department of Condensed Matter Physics, Weizmann Institute of Science, Rehovot 7610001, Israel. ²Catalan Institute of Nanoscience and Nanotechnology (ICN2), CSIC and the Barcelona Institute of Science and Technology, Campus UAB, Bellaterra, 08193 Barcelona, Spain. ³National Graphene Institute, The University of Manchester, Booth Street East, Manchester M13 9PL, UK. ⁴School of Physics and Astronomy, The University of Manchester, Manchester M13 9PL, UK. ⁵Department of Materials and Interfaces, Weizmann Institute of Science, Rehovot 7610001, Israel. ⁶Department of Physics, Massachusetts Institute of Technology, Cambridge, Massachusetts 02139, USA. [†]Present address: Department of Physics, Columbia University, New York, New York 10027, USA.

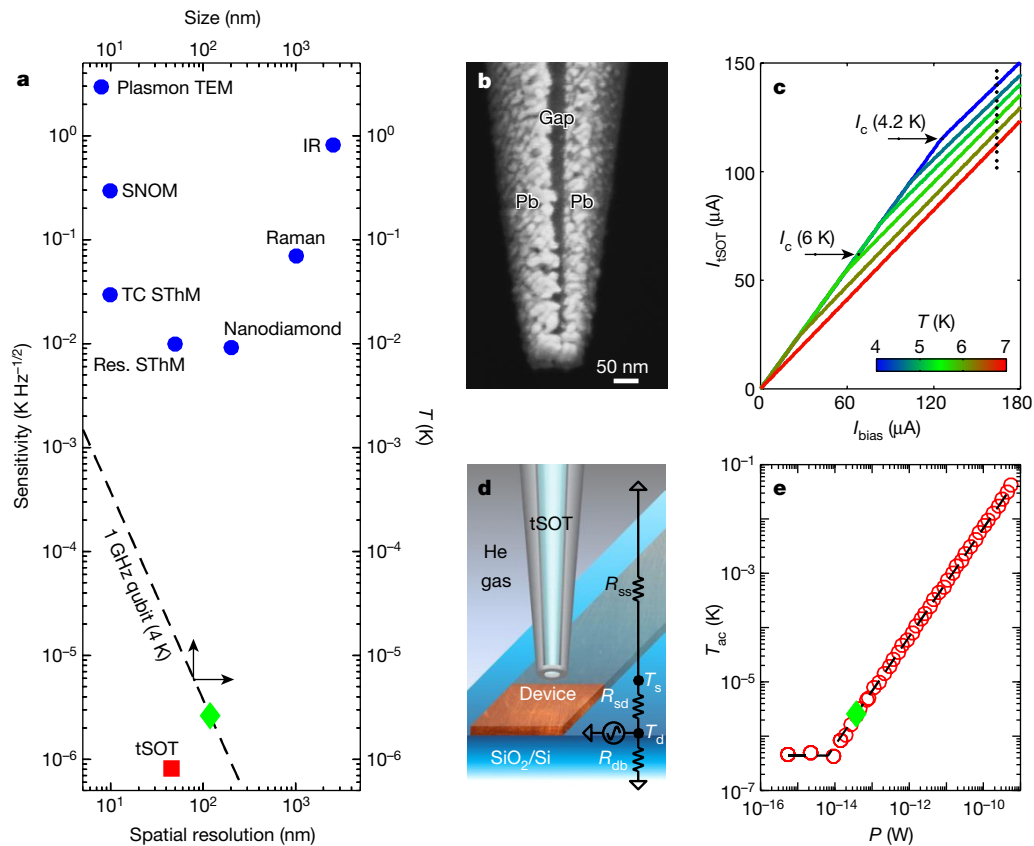


Figure 1 | tSOT characteristics and performance. **a**, Sensitivities (left-hand axis) of different thermal imaging techniques (blue) and of the tSOT (red) versus their spatial resolution (bottom axis). Green diamond, the measured temperature increase (right-hand axis) due to 40 fW dissipation (taken from **e**) corresponding to Landauer's limit for qubit operation at 4.2 K at 1 GHz along with the theoretical scaling of the temperature (right-hand axis) with the qubit size (dashed line, top axis). See main text for definitions of the thermal imaging techniques. **b**, SEM image of the 46-nm effective diameter Pb tSOT. **c**, Electrical characteristics of the tSOT

thermal resistance R_{ss} is required between the sensor and its support structure. The resulting overall requirement of $R_{\text{ss}} \gg R_{\text{sd}} \gg R_{\text{db}}$ is usually hard to achieve in AFM-type scanning thermal probes¹², leading to invasive in-contact imaging^{13,14}. In a tSOT, in contrast, R_{ss} is extremely high, owing to the unique nanoscale cross-section geometry of the device, giving rise to a quantum-limited phonon thermal conductivity²⁴, and to the absence of electronic heat conductivity along the superconducting leads. As a result, our smaller tSOT attains $R_{\text{ss}} \approx 10^{11} \text{ K W}^{-1}$ (see Supplementary Information section S6) as compared to $R_{\text{db}} \approx 10^7 \text{ K W}^{-1}$ for a $120 \text{ nm} \times 120 \text{ nm}$ device on a SiO_2/Si substrate at 4.2 K (Fig. 1e). The corresponding optimal R_{sd} of 10^8 to 10^{10} K W^{-1} is readily achieved in our configuration using a few mbar of He exchange gas to tune R_{sd} (Supplementary Fig. 8). These features permit non-contact sensing of the T_{d} of the sample with nanoscale resolution (Supplementary Fig. 2 and Supplementary Information sections S3, S4).

To characterize the thermal sensitivity of the scanning tSOT, we position the sensor above a 120-nm-wide Cu nanowire on a SiO_2/Si substrate (Fig. 1d and Supplementary Fig. 7); the nanowire is carrying an alternating current (a.c.), which results in an a.c. temperature modulation T_{ac} of the nanowire at 13.1 kHz. By changing the current amplitude, we measured tSOT T_{ac} versus the power P dissipated per square $120 \text{ nm} \times 120 \text{ nm}$ segment of the wire (Fig. 1e). Since $T_{\text{ac}} \ll T_{\text{b}}$, where $T_{\text{b}} = 4.2 \text{ K}$ is the thermal bath temperature, the measurement is in the small signal limit and hence T_{ac} is linear in P as expected, reaching a noise level of $T_{\text{ac}} \approx 440 \text{ nK}$ at $P \approx 6 \text{ fW}$. The green triangle in Fig. 1e shows the Landauer dissipation limit of $P = 40.2 \text{ fW}$ of a qubit operating

for temperatures ranging from 4.2 K to 7.2 K with marked values of the critical current I_c at representative temperatures. **d**, Schematic drawing of the measurement set-up and a simplified effective thermal circuit. See main text for definitions of symbols. **e**, Measurement of the tSOT temperature T_{ac} at 13.1 kHz above a 120-nm-wide Cu nanowire with sheet resistance 0.46Ω per square versus the a.c. power P dissipated by a variable I_{ac} in a $120 \text{ nm} \times 120 \text{ nm}$ unit segment of the nanowire. The dashed line shows a linear fit (with slope $R_{\text{db}} = 6.8 \times 10^7 \text{ K W}^{-1}$) and a noise floor of $T_{\text{ac}} \approx 440 \text{ nK}$ below $P \approx 6 \text{ fW}$ using a lock-in amplifier time constant of 1 s.

at 1 GHz at 4.2 K, which gives rise to $T_{\text{ac}} = 2.6 \mu\text{K}$ in our sample. This value is indicated in Fig. 1a (green triangle) along with the expected inverse scaling of the qubit temperature with its area (dashed line).

By applying a proper combination of magnetic field and bias, the tSOT can be tuned to have both magnetic field and thermal sensitivities. As the Oersted field generated by the transport current in the sample is linear in current while the dissipation is quadratic, the resulting magnetic field signal B_z^{ac} generated by the a.c. current I_{ac} at frequency f can be imaged simultaneously with the thermal signal T_{ac} that will be present at frequency $2f$, as shown in Supplementary Fig. 11.

We used the tSOT for nanoscale thermal imaging of quantum matter. Figure 2a, b shows T_{ac} images of two single-walled carbon nanotubes (CNTs) carrying an alternating current of few nA. Each CNT is wound into a loop²⁵, as outlined by the dotted trajectories and shown by SEM images in Fig. 2d, e. The thermal signal in Fig. 2a tracks the CNT, revealing the current-driven dissipation along the entire length of the CNT. Surprisingly, and in contrast to the above, Fig. 2b shows an absence of heating in the circular part of the loop. The T_{ac} image thus reveals that the applied current bypasses the loop, exposing an electrically shorted junction between the two crossing sections of the CNT. This observation illustrates the capacity of the tSOT for fault detection in operating nanodevices.

A striking feature evident in Fig. 2a, b is ring-like fine structure: a zoomed-in T_{ac} image of one of these is shown in Fig. 2c. These features resemble the Coulomb blockade rings observed in scanning gate microscopy²⁶, in which the conductance through a quantum dot is measured as a function of the position of a conducting AFM tip. In the

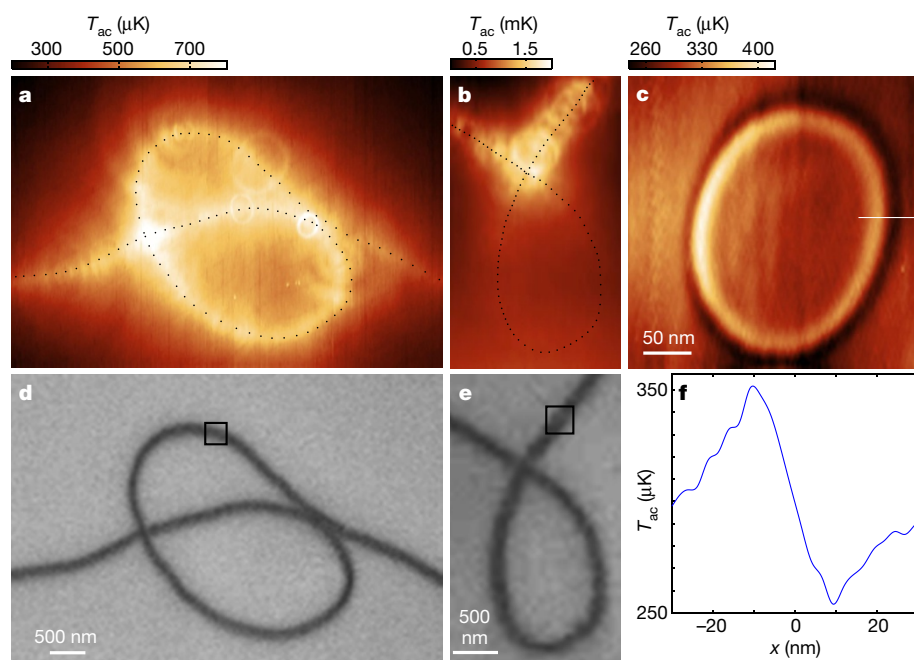


Figure 2 | Thermal imaging of single-walled CNTs and scanning gate thermometry of quantum dots. **a, b,** Thermal images of two CNT devices with loop geometry carrying I_{ac} of 12 nA (**a**) and 3 nA (**b**), revealing an electrical short at the loop intersection point in **b**. The colour scale used for T_{ac} is shown at the top of each image. The $T_{ac}(x, y)$ was acquired by a tSOT of 104-nm diameter at scanning heights of about 65 nm (**a**) and 150 nm (**b**). The ring-like structures in T_{ac} result from variations in dissipation due to modulations in the single-electron charging of individual quantum dots as described for **c**. **c,** Zoomed-in scanning gate thermometry image of a single quantum dot in the area boxed in **d** at a scan height of about 35 nm (T_{ac} scale at top). Variations in the electrochemical potential of the quantum dot induced by the scanning tSOT give rise to changes of the temperature of the dot at the Coulomb blockade peak conditions along the equipotential ring-like contour. **d, e,** SEM images of the devices in **a** and **b**. Boxed area in **e** is shown in Supplementary Fig. 15. **f,** Line-cut across the line marked on right in **c**.

case of scanning gate microscopy, the characteristic equipotential rings (corresponding to the periodic conditions of Coulomb blockade peaks governed by single-electron charging of the quantum dot²⁷) originate from the tip acting as a local gate. Since the tSOT is conducting, it can also serve as a nanoscale scanning gate. The disordered substrate potential in our long CNTs on the SiO₂/Si substrate gives rise, however, to carrier localization and formation of a series of electronic quantum dots, resulting in CNT resistances in excess of 10 MΩ. As a result, no detectable change in CNT conductance is observed while scanning the tSOT. The unique feature of the tSOT, however, is that in addition to functioning as a scanning gate it simultaneously operates as a nanoscale thermometer that detects minute changes in the local dissipation resulting from its own controllable local gating. The T_{ac} ring in Fig. 2c with a cross-sectional width of 20 nm (Fig. 2f) thus reveals microkelvin-range changes of the temperature of a quantum dot resulting from the modulation of its single-electron Coulomb blockade conductance peaks by the scanning tSOT (see Supplementary Information sections S13, S14 for additional details). This novel ‘scanning gate thermometry’ thus adds another functionality to the tSOT, allowing nanoscale manipulation of the potential and study of the induced changes in the local scattering processes and dissipation that are inaccessible by other methods.

One of the topics of great interest in the study of electronic transport at low temperatures is the non-equilibrium heating of the electron bath and the proliferation of hot carriers due to poor electron–phonon

coupling. Graphene offers a unique system in which the typical distance for such carrier–lattice cooling can exceed the dimensions of the device²⁸ owing to the anomalously long lifetime of the hot carriers²⁹. Electron cooling rates are believed to be sharply enhanced in the presence of disorder, but the precise mechanism of such enhancement is poorly understood³⁰.

To probe microscopic dissipation mechanisms in graphene, we performed scanning thermometry in high-mobility graphene encapsulated in hexagonal boron nitride (hBN). We used a washer-shaped device to which a direct current was applied between top and bottom constrictions, as illustrated in Fig. 3a (see Supplementary Information section S12 for details). Figure 3b shows the corresponding scanning gate thermal image, revealing a startling visualization of dissipation processes, which are manifested in a complex structure of two ‘necklaces’ of rings along the inner and outer edges of the device. The sharp ring-like structures have the same origin as the ring-like patterns in the CNTs in Fig. 2a–c, and reveal the presence of localized resonant states at the edges of the graphene; these states are acting as atomic-scale heat beacons. The tSOT functions as a top gate, which tunes the potential of the localized states into resonance when the combination of its distance and the voltage V_{tSOT} applied between the tip and the sample match the resonance conditions. This gives rise to sharp rings of enhanced temperature, as described in detail in Supplementary Information sections S13 and S15. Consequently, the ring radius R changes

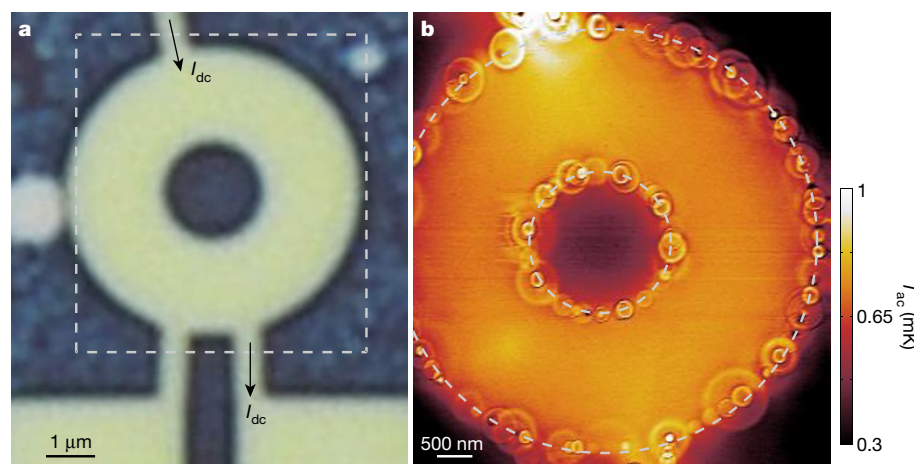


Figure 3 | Scanning gate thermometry of dissipation at localized resonant states at graphene edges. **a,** Optical image of hBN/graphene/hBN structure patterned into a washer shape (bright) with inner and outer diameters of 2 μm and 6 μm, respectively. Arrows show where the direct current I_{dc} was applied. **b,** Scanning a.c. gate thermometry T_{ac} image of the boxed area in **a** in the presence of $I_{dc} = 6 \mu A$ at a carrier concentration of 10^{12} cm^{-2} ; the T_{ac} colour scale is shown on right. The $T_{ac}(x, y)$ was acquired by a tSOT of 100-nm diameter at 4.2 K at a height of 40 nm in the presence of an a.c. potential of 200 mV applied to the tip (see Supplementary Information sections S13–S15). The dashed lines mark graphene edges. The ‘necklace’ of rings reveals the presence of resonant states along the edges of graphene that serve as local centres of energy dissipation.

on varying V_{tSOT} , as demonstrated in Supplementary Fig. 16 and Supplementary Video S1, or on changing the tip height, as demonstrated in the case of a CNT in Supplementary Fig. 15.

Despite the similarity between the ring-like structures observed in CNTs and in graphene, their microscopic origin appears to be different. For CNTs, the disorder potential creates quantum dots that confine discrete electronic states. Since the conductance of the quantum dot is sharply enhanced under resonant conditions, the Coulomb blockade staircase gives rise to the sequence of concentric rings of enhanced local temperature in the presence of current flow through the CNT (Supplementary Fig. 15). In our hBN/graphene/hBN devices, in contrast, the hot electrons flow mainly in the bulk of the graphene, while electron–lattice cooling occurs predominantly at defect states at graphene edges. Such defects can be formed by the vacancies and adatoms produced at the exposed graphene edges during the etching process. Spatially localized electronic states originating from such defects, with energies pinned to the Dirac point³¹, were recently revealed by scanning tunnelling microscopy³². Localized states can considerably enhance electron–phonon coupling, thus providing a local drain for the excess energy of the hot electrons³⁰. Since each defect creates a single resonant electronic state³¹, only one ring should be observed around each defect with radius R that depends on V_{tSOT} , as shown in Supplementary Fig. 16 and Supplementary Video S1. Acting as gate-tunable spatially localized energy flow bottlenecks, these dissipation centres are likely to play a dominant role in the hot-carrier applications of graphene electronics. These observations shed new light on electron–lattice cooling mechanisms in graphene.

The observation of striking, spatially localized dissipation centres at graphene edges underscores the potential of the tSOT technique for uncovering the microscopic origins of dissipation in novel states of matter. Other systems of interest are topologically protected surface states, edge states in quantum spin and anomalous quantum Hall systems, and surface states in Weyl semimetals. By choosing appropriate superconducting materials^{22,23,33}, it should be possible to extend the operating temperature range of the tSOT from tens of millikelvin to tens of kelvin (Supplementary Fig. 1d), thus allowing investigation of a wide range of quantum systems. In addition, the operation of the tSOT at elevated magnetic fields combined with the multifunctional abilities of magnetic sensing and scanning gate thermometry opens the way to nanoscale investigation and imaging of intricate thermoelectric and thermomagnetic phenomena. These include the Nernst effect, the thermal Hall effect, thermoelectric nanoscale cooling and quantum heat conductance.

Received 25 November 2015; accepted 31 August 2016.

Published online 26 October 2016.

1. Yue, Y. & Wang, X. Nanoscale thermal probing. *Nano Rev.* **3**, 11586 (2012).
2. Giazotto, F., Heikkilä, T. T., Luukanen, A. M. & Pekola, J. P. Opportunities for mesoscopies in thermometry and refrigeration: physics and applications. *Rev. Mod. Phys.* **78**, 217–274 (2006).
3. Jin, C. Y., Li, Z., Williams, R. S., Lee, K. C. & Park, I. Localized temperature and chemical reaction control in nanoscale space by nanowire array. *Nano Lett.* **11**, 4818–4825 (2011).
4. Kucsko, G. *et al.* Nanometre-scale thermometry in a living cell. *Nature* **500**, 54–58 (2013).
5. Mecklenburg, M. *et al.* Nanoscale temperature mapping in operating microelectronic devices. *Science* **347**, 629–632 (2015).
6. Teyssieux, D., Thiery, L. & Cretin, B. Near-infrared thermography using a charge-coupled device camera: application to microsystems. *Rev. Sci. Instrum.* **78**, 034902 (2007).
7. Toyli, D. M., de las Casas, C. F., Christle, D. J., Dobrovitski, V. V. & Awschalom, D. D. Fluorescence thermometry enhanced by the quantum coherence of single spins in diamond. *Proc. Natl Acad. Sci. USA* **110**, 8417–8421 (2013).
8. Neumann, P. *et al.* High-precision nanoscale temperature sensing using single defects in diamond. *Nano Lett.* **13**, 2738–2742 (2013).
9. Reparaz, J. S. *et al.* A novel contactless technique for thermal field mapping and thermal conductivity determination: two-laser Raman thermometry. *Rev. Sci. Instrum.* **85**, 034901 (2014).
10. Brites, C. D. S. *et al.* Thermometry at the nanoscale. *Nanoscale* **4**, 4799–4829 (2012).

11. Majumdar, A. Scanning thermal microscopy. *Annu. Rev. Mater. Sci.* **29**, 505–585 (1999).
12. Menges, F. *et al.* Temperature mapping of operating nanoscale devices by scanning probe thermometry. *Nat. Commun.* **7**, 10874 (2016).
13. Kim, K., Jeong, W., Lee, W. & Reddy, P. Ultra-high vacuum scanning thermal microscopy for nanometer resolution quantitative thermometry. *ACS Nano* **6**, 4248–4257 (2012).
14. Sadat, S., Tan, A., Chua, Y. J. & Reddy, P. Nanoscale thermometry using point contact thermocouples. *Nano Lett.* **10**, 2613–2617 (2010).
15. Grosse, K. L., Bae, M. H., Lian, F., Pop, E. & King, W. P. Nanoscale Joule heating, Peltier cooling and current crowding at graphene–metal contacts. *Nat. Nanotechnol.* **6**, 287–290 (2011).
16. Pekola, J. P. Towards quantum thermodynamics in electronic circuits. *Nat. Phys.* **11**, 118–123 (2015).
17. Landauer, R. Irreversibility and heat generation in the computing process. *IBM J. Res. Develop.* **5**, 183–191 (1961).
18. Bérut, A. *et al.* Experimental verification of Landauer’s principle linking information and thermodynamics. *Nature* **483**, 187–189 (2012).
19. Herr, Q. P., Herr, A. Y., Oberg, O. T. & Ioannidis, A. G. Ultra-low-power superconductor logic. *J. Appl. Phys.* **109**, 103903 (2011).
20. Kuhn, K. J. *et al.* The ultimate CMOS device and beyond. *IEEE Int. Electron Devices Meet.* 8.1.1–8.1.4 (2012).
21. Faivre, T., Golubev, D. & Pekola, J. P. Josephson junction based thermometer and its application in bolometry. *J. Appl. Phys.* **116**, 094302 (2014).
22. Vasyukov, D. *et al.* A scanning superconducting quantum interference device with single electron spin sensitivity. *Nat. Nanotechnol.* **8**, 639–644 (2013).
23. Finkler, A. *et al.* Self-aligned nanoscale SQUID on a tip. *Nano Lett.* **10**, 1046–1049 (2010).
24. Schwab, K., Henriksen, E. A., Worlock, J. M. & Roukes, M. L. Measurement of the quantum of thermal conductance. *Nature* **404**, 974–977 (2000).
25. Shadmi, N., Geblinger, N., Ismach, A. & Joselevich, E. Formation of ordered vs disordered carbon nanotube serpentine on anisotropic vs isotropic substrates. *J. Phys. Chem. C* **118**, 14044–14050 (2014).
26. Woodside, M. T. & McEuen, P. L. Scanned probe imaging of charge states in nanotube quantum dots. *Science* **296**, 1098–1101 (2002).
27. Grabert, H. & Devoret, M. H. (eds) *Single Charge Tunneling: Coulomb Blockade Phenomena in Nanostructures* (Vol. 294, NATO Sci. Ser. B, Springer, 2013).
28. Bandurin, D. A. *et al.* Negative local resistance caused by viscous electron backflow in graphene. *Science* **351**, 1055–1058 (2016).
29. Bistritzer, R. & MacDonald, A. H. Electronic cooling in graphene. *Phys. Rev. Lett.* **102**, 206410 (2009).
30. Song, J. C. W., Reizer, M. Y. & Levitov, L. S. Disorder-assisted electron-phonon scattering and cooling pathways in graphene. *Phys. Rev. Lett.* **109**, 106602 (2012).
31. Pereira, V. M., Guinea, F., Lopes dos Santos, J. M. B., Peres, N. M. R. & Castro Neto, A. H. Disorder induced localized states in graphene. *Phys. Rev. Lett.* **96**, 036801 (2006).
32. González-Herrero, H. *et al.* Atomic-scale control of graphene magnetism by using hydrogen atoms. *Science* **352**, 437–441 (2016).
33. Lachman, E. *et al.* Visualization of superparamagnetic dynamics in magnetic topological insulators. *Sci. Adv.* **1**, e1500740 (2015).

Supplementary Information is available in the online version of the paper.

Acknowledgements We thank A. F. Young for discussions, M. V. Costache and S. O. Valenzuela for facilitation of fabrication of permalloy (Py)/copper (Cu) samples that were used in Supplementary Information section S9, D. Shahar, I. Tamir, T. Levinson and S. Mitra for assistance in fabrication of a:In₂O₃ integrated devices that were used in Supplementary Information section S2, M. E. Huber for SOT readout setup, and M. L. Rappaport for technical assistance. This work was supported by the European Research Council (ERC) under the European Union’s Horizon 2020 programme (grant no. 655416), by the Minerva Foundation with funding from the Federal German Ministry of Education and Research, and by a Rosa and Emilio Segré Research Award. L.S.L. and E.Z. acknowledge the support of the MISTI MIT-Israel Seed Fund.

Author Contributions D.H., J.C. and E.Z. conceived the technique and designed the experiments. D.H. and J.C. performed the measurements. D.H. performed the analysis and theoretical modelling. L.E. constructed the scanning SOT microscope. M.B.S. and A.K.G. designed and provided the graphene sample and contributed to the analyses of the results. N.S. and E.J. fabricated the CNT samples. J.C. fabricated the Cu/Py sample. D.H., H.R.N. and J.S. fabricated the a:In₂O₃ sample. D.H. and Y.R. designed and fabricated the spatial resolution demonstration sample. H.R.N., Y.A. and A.U. fabricated the tSOT sensors. Y.A. and Y.M. developed the SOT fabrication technique. A.U., Y.M. and D.H. developed the tuning-fork based tSOT height control technique. L.S.L. performed theoretical analysis. D.H., J.C. and E.Z. wrote the manuscript. All authors participated in discussions and writing of the manuscript.

Author Information Reprints and permissions information is available at www.nature.com/reprints. The authors declare no competing financial interests. Readers are welcome to comment on the online version of the paper. Correspondence and requests for materials should be addressed to D.H. (dorri.halbental@weizmann.ac.il) or E.Z. (eli.zeldov@weizmann.ac.il).

Reviewer Information Nature thanks I. Maasilta, S. Volz and the other anonymous reviewer(s) for their contribution to the peer review of this work.